THE JOURNAL OF PHYSICAL CHEMISTRY Letters

Cite This: J. Phys. Chem. Lett. 2019, 10, 7942−7948

Letter

pubs.acs.org/JPCL

Investigation of Chemical Origin of White-Light Emission in Two-Dimensional $(C_4H_9NH_3)_2PbBr_4$ via Infrared Nanoscopy

Dae Young Park,[†,⊥] Sung-Jin An,[†,‡,⊥] Chanwoo Lee,[†,‡] Duc Anh Nguyen,[†] Kang-Nyeoung Lee,[†] and Mun Seok Jeong*[,†,‡]

[†]Department of Energy Science, Sungkyunkwan University, Suwon 16419, Republic of Korea

[‡]Center for Integrated Nanostructure Physics (CINAP), Institute for Basic Science (IBS), Suwon 16419, Republic of Korea

Supporting Information

ABSTRACT: The broadband light emission in low-dimensional organic lead halide perovskites (OHPs) is a fascinating property for white light-emitting diodes (LEDs). However, unique emission has been observed in highly distorted low-dimensional OHPs such as (110) and (111) perovskites. Herein, we report the first observation of white-light emission under ambient (21 °C) conditions in a rectangular microsheet of $(C_4H_9NH_3)_2PbBr_4$, a (100) perovskite. The origin of white-light emission in $(C_4H_9NH_3)_2PbBr_4$ was revealed as defect-assisted radiative recombination via excitation power-dependent photoluminescence measurement. Additionally, the origin of the defect was confirmed to be organic cation vacancies formed by intercalated water molecules via infrared nanoscopy. This result can help to improve the performance of white LEDs using low-dimensional OHPs.

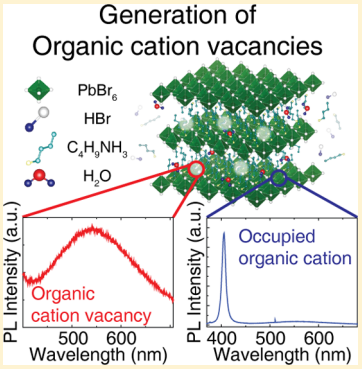

Organic lead halide perovskites (OHPs) with the chemical formula ABX_3 are emerging materials in photovoltaics and light-emitting diodes (LEDs) owing to their excellent optoelectronic properties (A = organic cation, B = lead, X = halides).[1−3] The simple controllability of the constituents allows the formation of diverse OHP crystal structures with different optoelectronic properties.[4−7] In particular, low-dimensional OHPs have the advantages of higher quantum yield and better moisture stability than three-dimensional (3D) structures.[8] The large organic cations in OHPs can separate the lead halide framework along a certain crystal direction, forming low-dimensional OHPs with two-dimensional (2D), one-dimensional, and zero-dimensional inorganic frameworks called (100), (110), and (111) perovskites, respectively.[8] Interestingly, unique broadband light emission under ambient (21 °C) conditions is observed in low-dimensional OHPs, except for (100) perovskites.[9−12] When the excessive electrons originating from free excitons are introduced to a highly polar 3D crystal, the Coulomb interaction between the electrons and the lattices strengthens the electron−phonon coupling. The electrons are delocalized over several lattices to produce reversible lattice deformation and large polarons.[13−15] In the case of 3D OHPs such as $CH_3NH_3PbX_3$, these optical signatures are detected in the terahertz range.[16] However, low-dimensional OHPs can confine the polarons within limited inorganic frameworks, and the polaronic characteristics strongly depend on the local lattice properties owing to the small polaron size.[17,18] Accordingly, unique broadband light emission in (110) and (111) perovskites is induced by the multiple polaron−exciton states formed in the highly confined inorganic lattice.[9−12] The structural origin of the distinct emission stems from equatorial lead-halide bond angle tilting in OHPs. An equatorial bond angle of <150° resulting from notable steric hindrance generates an interesting polaron property, i.e., the self-trapping of electron or hole states (STE or STH) in (110) and (111) perovskites.[10,19,20] Meanwhile, for (110) and (111) perovskites having highly tilted inorganic frameworks, large Rashba band splitting has been reported.[21,22] The Rashba band splitting in OHPs generates an indirect bandgap pathway of radiative recombination, reducing the photoluminescence (PL) quantum yields of OHPs.[23] Therefore, small tilted PbX_6 octahedrons, such as (100) perovskite, have great potential for white LEDs owing to the suppression of the Rashba band splitting.

In this work, we observed broadband emission from $(C_4H_9NH_3)_2PbBr_4$ ($C_4H_9NH_3$ = BuA) microplates, i.e., (100) perovskite, at room temperature (21 °C). The origin of the broadband emission was investigated through excitation power-dependent PL measurements. We observed that the white-light emission in $(BuA)_2PbBr_4$ arose from defect-assisted radiative recombination. To investigate the origin of the defects, infrared (IR) spectroscopy was conducted at the nanoscale, i.e., IR nanoscopy. According to the IR nanoscopy data, intercalated water molecules generated organic cation vacancies via the degradation process and induced lattice deformation. Compared with polarons, organic cation

Received: November 11, 2019
Accepted: December 9, 2019
Published: December 9, 2019

DOI: 10.1021/acs.jpclett.9b03328
J. Phys. Chem. Lett. 2019, 10, 7942−7948

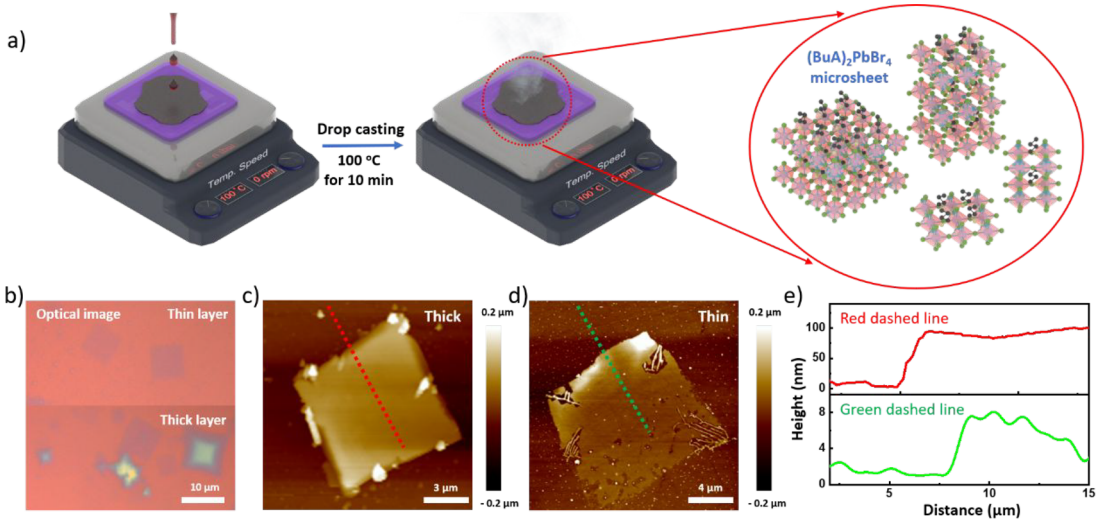

Figure 1. Formation and morphology of $(BuA)_2PbBr_4$ microsheets. (a) Schematic of the sample preparation. (b) Optical image of as-grown $(BuA)_2PbBr_4$ microsheets. The AFM measurement results for (c) thick and (d) thin sheets. (e) Line profiles corresponding to panels c and d.

vacancies as a permanent form of lattice deformation exhibited similar broadband emission in the (100) perovskite.

Square $(BuA)_2PbBr_4$ microsheets were prepared via a previously reported method with some modifications. To form rectangular 2D sheets, the concentration and mixing ratio of solvents with OHPs differing in solubility were controlled carefully in the ternary cosolvent system in Figure 1a.[24] First, we examined the effect of the solution concentration on the $(BuA)_2PbBr_4$ morphology in a binary system of dimethyl sulfoxide (DMSO) and acetonitrile. A highly concentrated solution (35 mM) formed a large-grain film owing to the layered crystal structure, as shown in Figure S1a. When we reduced the concentration, the particle-like aggregates changed, as shown in Figure S1b,c. Thus, we concluded that the optimal concentration for the proper shape and size of $(BuA)_2PbBr_4$ was close to 0.35 mM. Then, the poor solvent effect in the ternary cosolvent system with chlorobenzene or toluene was optimized. A poor solvent is important for crystallizing the square $(BuA)_2PbBr_4$ through the ligand-exchange reaction with DMSO.[25] As the amount of the poor solvent increased, the shape of the $(BuA)_2PbBr_4$ was changed from irregular islands to rectangles approximately 10 μm long, as shown in Figure S2. The polarities of the organic solvents determined the rate of solvent mixing. Organic solvents with similar polarities can mix more rapidly than those with different polarities. Because of different relative polarities of chlorobenzene (0.188), toluene (0.099), and DMSO (0.444), the optimized antisolvent volume for 0.5 mL of the $(BuA)_2PbBr_4$ solution (0.73 mM) was 0.3 mL of chlorobenzene and 0.4 mL of toluene. OHP is a strong ionic compound that can be dissolved in highly polar organic solvents such as DMSO.[26] Additionally, strong metal−ligand interaction between Pb^{2+} ions and DMSO can facilitate the uniform formation of 2D $(BuA)_2PbBr_4$ through ligand exchange in the presence of chlorobenzene or toluene having poor solubility.[27] When acetonitrile, which has an intermediate solubility between those of DMSO and chlorobenzene, was introduced, uniform square $(BuA)_2PbBr_4$ microsheets were successfully grown on the substrate. The rectangular $(BuA)_2PbBr_4$ sheets approximately 10 μm long exhibited different colors owing to the thickness variation, as shown in Figure 1b. To examine the morphology of the microsheets, atomic force microscopy (AFM) was performed. The d spacing of bulk $(BuA)_2PbBr_4$ (1.4 nm calculated using XRD data in Figure 2a) represents the thickness of the $(BuA)_2PbBr_4$ monolayer.[24] The AFM measurement results for thick and thin plates are shown in panels c and d of Figure 1, respectively. As shown in Figure 1c, the white particle was rolled by the AFM tip. It scratches the sample while the AFM tip scans steep edges of the sample. The line profiles indicate that they had thicknesses of 100 nm (~70 layers) and 8 nm (5−6 layers) in Figure 1e.

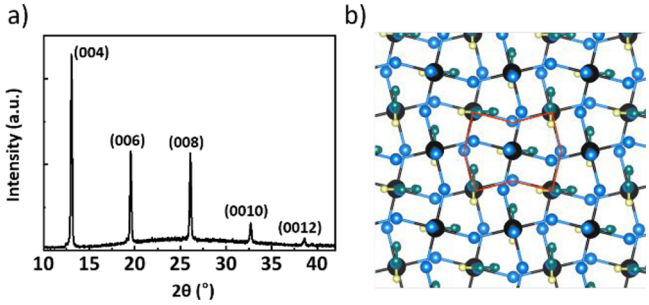

Figure 2. (a) XRD measurement for identifying the $(BuA)_2PbBr_4$ crystal structure. (b) Fragment of the $(BuA)_2PbBr_4$ crystal structure.

To examine the crystal structure, the as-grown $(BuA)_2PbBr_4$ was measured using an X-ray diffraction (XRD) diffractometer in Figure 2a. Clear (00l) diffraction peaks (l = even) were observed, indicating that the perovskite layers were aligned along the z-axis (layered structure). Using the diffraction peak at 13.05° corresponding to (004) diffraction plane and Bragg's law ($n\lambda = 2d \sin\theta$), the d spacing value was calculated to be 1.4 nm. Additionally, lattice parameter c was also calculated to be 2.711 nm using the calculated d spacing value (1.4 nm) of the (004) diffraction plane and the d spacing equation of orthorhombic structure ($\frac{1}{d^2} = \frac{h^2}{a^2} + \frac{k^2}{b^2} + \frac{l^2}{c^2}$), where a, b, and c are lattice parameters and h, k, and l are Miller indices, respectively. The calculated structural information on $(BuA)_2PbBr_4$ microsheet such as d spacing value (1.4 nm) and lattice parameter c (2.711 nm) were in agreement with previously reported structural result.[24] To understand the

DOI: 10.1021/acs.jpclett.9b03328
J. Phys. Chem. Lett. 2019, 10, 7942−7948

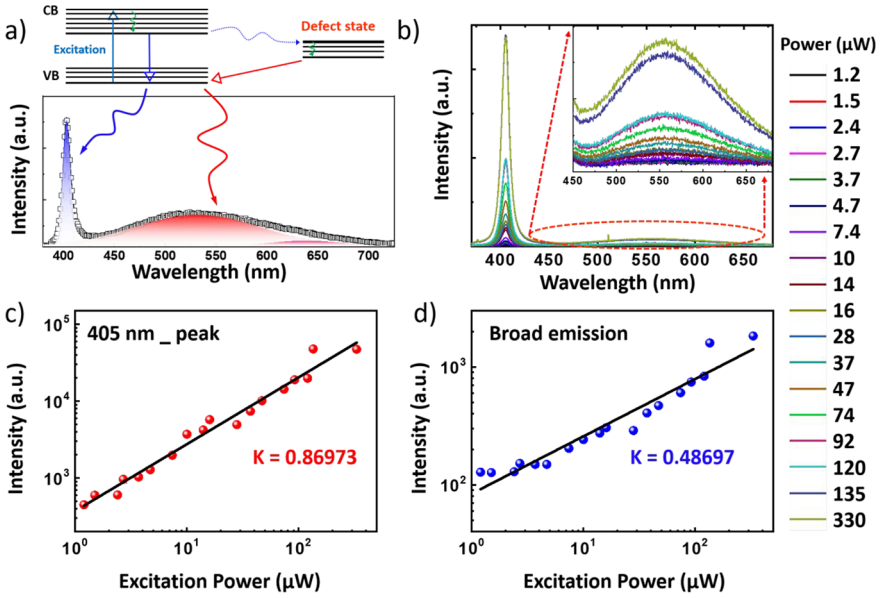

Figure 3. Excitation power-dependent PL measurement. (a) Schematic of the origin of PL emission at 405 nm and in the broadband region and an energy-level diagram of the typical excitonic and band-to-band transitions of 2D perovskites. (b) PL spectra obtained using a 355 nm excitation laser. The inset shows the broadband emission spectra extracted from a specific region marked by a red solid line. (c and d) Variation of the PL intensities at 405 nm and in the broadband emission region depending on the laser power.

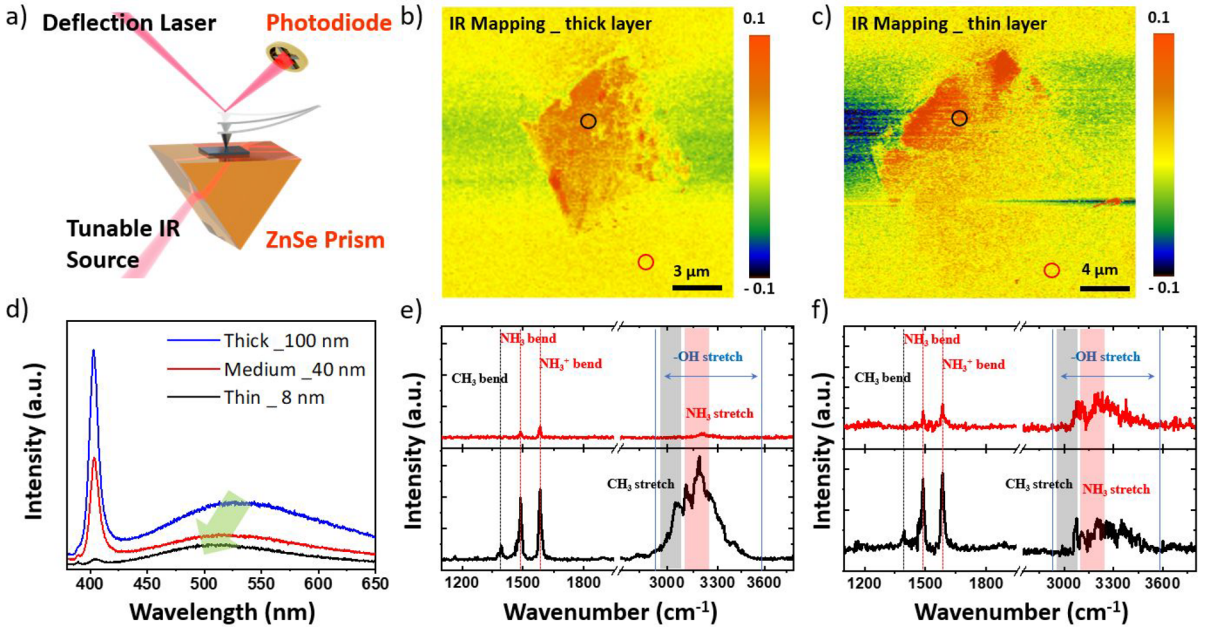

Figure 4. Analysis of the optical properties via IR nanoscopy and PL measurements. (a) Schematic of the IR nanoscopy. The mapping images of (b) thick and (c) thin $(BuA)_2PbBr_4$. (d) PL spectra of the OHP depending on the thickness. (e and f) Absorption spectrum of $(BuA)_2PbBr_4$ extracted from the mapping images, corresponding to the red and black circles in panels b and c.

crystal structure of as-prepared 2D perovskite, Figure 2b shows fragment of the $(BuA)_2PbBr_4$. Many studies have explained the broadband emission of 2D OHP arising from the combination of confined small polarons and a local crystal structure. For the formation of a small polaron, a delocalized electron should be confined in small PbX_3 octahedrons.[9−12,17,18] In the case of 2D perovskites, the movement of the electrons along the *z*-axis can be prevented by large insulating organic cations. Additionally, large organic cations satisfy the specific crystal structure.

The structural requirement combining small polarons for unique emission is a distorted equatorial Pb−X bond angle of <150°.[10,19,20] Therefore, many perovskites with broadband emission have large organic cations, such as phenethylammonium, N-(3-aminopropyl) imidazole, and $(NH_3(CH_2)_2O(CH_2)_2O(CH_2)_2NH_3)^{2+}$, for large equatorial distortion of inorganic frameworks less than 150°. In contrast, the equatorial Pb−Br bond angle of $(BuA)_2PbBr_4$ is 152°, which is insufficient for generating broadband emission.[8,9,11,24,28] However, the as-grown thick $(BuA)_2PbBr_4$ microsheet under inert atmosphere conditions exhibits two distinct PL peaks: a sharp peak at 405 nm and a broad peak from 450 to 700 nm centered around 550 nm (Figure 3a). The electron emission

DOI: 10.1021/acs.jpclett.9b03328
J. Phys. Chem. Lett. 2019, 10, 7942−7948

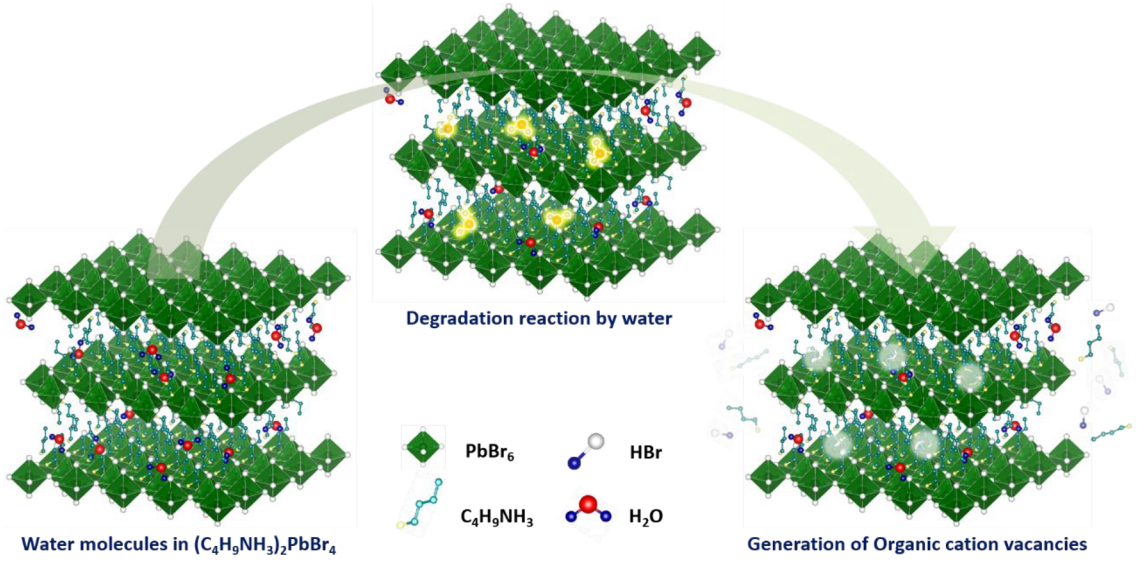

Figure 5. Schematic of the water-assisted degradation mechanism in $(BuA)_2PbBr_4$ microsheets.

peak (405 nm) is the characteristic exciton emission resulting from the two-dimensional $PbBr_4$ layer in the perovskite compound. Besides, the broadband emission is identical to the white-light emission in low-dimensional perovskites with a broad peak shape having a Stokes shift above 1 eV.[8,29,30] We performed laser power-dependent PL measurements to investigate the origin of the broadband emission (~550 nm) and the sharp PL peak at 405 nm. Figure 3b shows the PL spectra of $(BuA)_2PbBr_4$ sheets (~70 layers) with various excitation powers ranging from 1.2 to 330 μW under inert atmosphere conditions. Generally, radiative recombination can occur from exciton-like transitions, free-to-bound transitions, band-to-band transitions, and donor–acceptor pair transitions.[31,32] We can estimate the origin of broadband emission from $(BuA)_2PbBr_4$ in the 550 nm region using the power-law equation of the excitation power and PL intensity as follows:

$$I_{PL} = nI_L^k \quad (1)$$

where I represents the PL intensity. L represents the excitation power, and n represents the emission efficiency; the exponent k indicates the recombination mechanism. The range of k values is 1–2 for free or bound exciton recombination and <1 for impurity-related recombination. These processes are related to the neutral impurities caused by the photoneutralization of the donor–acceptor pair, which appear in all semiconductor materials. The coefficient k = 2 is related to band-to-band recombination.[32,33] Panels c and d of Figure 3 show the increase in the PL intensity depending on the laser power. The fitted k values of the 405 nm peak and broadband emission were 0.8697 and 0.4869, respectively. These results indicate that the broadband emission centered at 550 nm was due to the deep gap state induced by the vacancy defect.

We confirmed the chemical composition of the $(BuA)_2PbBr_4$ microsheets using IR absorption spectroscopy combined with AFM. For IR nanoscopy, the thermal expansion of the material was used, in contrast to other general Fourier transform infrared absorption analysis methods.[34,35] When the sample absorbs IR radiation, thermal energy leads to the rapid thermal expansion of the material in the illuminated region. This rapid thermal expansion is detected by changing the vibration frequencies of the AFM cantilever, as shown in Figure 4a. The observed ring-down motions of the tip were analyzed via a Fourier transform to extract the amplitudes and frequencies of the vibrations.[36] This technique can reveal the structural and chemical properties of a sample simultaneously, at a scale of tens of nanometers. Using this system, we investigated the vibrations of butyl ammonium in $(BuA)_2PbBr_4$ (CH_3 bending, NH_3 bending, and CH_3' bending) and the OH bonding (~3200 cm^{-1}) related to water molecules depending on the material thickness.[37−39] Panels b and c of Figure 4 show the absorption mapping images obtained using IR nanoscopy with a fixed 3200 cm^{-1} (3.125 μm) excitation laser from a tunable IR source. The black and red colored spectra in Figure 4e,f were extracted from the circled areas in Figure 4b,c. Strong peaks of CH_3 and NH_3 from the organic cations were detected in the $(BuA)_2PbBr_4$-covered area. However, the same vibration peaks were also observed with low intensities owing to individual organic cation residues that could not be detected by AFM. In the case of a thin flake, the intensity of the absorption peak from water molecules at ~3200 cm^{-1} did not change significantly over the whole area. Additionally, the $(BuA)_2PbBr_4$ microsheet exhibited an exponentially strong signal at approximately 3200 cm^{-1} when the sample thickness increased. Generally, water molecules can be absorbed physically on the surface of a zinc-selenide (ZnSe) prism or a $(BuA)_2PbBr_4$ sheet. However, in the case of thick $(BuA)_2Pbr_4$, the increase in the OH stretching intensity depending on the thickness indicated that the water molecules not only were absorbed on the surfaces but also penetrated the van der Waals gaps of the $(BuA)_2PbBr_4$ sheets owing to the strong hydrogen interaction between the halide and water. Thus, the thick sheet had many spaces to store water molecules.[40] To determine the changes of the white-light emission depending on the thickness of the $(BuA)_2PbBr_4$ sheet, we measured the PL using confocal PL spectroscopy with a 375 nm wavelength excitation laser. Each sample is specified in the legend of Figure 4d. The PL measurements of the $(BuA)_2PbBr_4$ sheets with different thicknesses indicated that the PL intensities were proportional to the thickness. The blue shift of the white-light emission was probably due to the structural relaxation of the in-plane crystal lattice.[41] A slight increase in the in-plane lattice constant for the few-layer

DOI: 10.1021/acs.jpclett.9b03328
J. Phys. Chem. Lett. 2019, 10, 7942−7948

samples was observed, compared with the bulk crystal, and the lattice expansion should have led to a small increase in the bandgap. With the increasing thickness, the amount of organic cation vacancies increased, resulting in stronger white-light emission for the $(BuA)_2PbBr_4$. With the degradation reaction with water and organic cations, we expect that organic cation vacancies can be generated in both surface and internal regions. These organic cation vacancies can contribute to the broadband emission in $(BuA)_2PbBr_4$ because they are among the irreversible lattice deformations.[42]

Numerous studies have been performed on the severe degradation of OHPs under ambient conditions.[43−46] Moisture is the most significant factor that destroys the perovskite structure. Thus, we propose the generation of organic vacancies in $(BuA)_2PbBr_4$ sheets based on a previously reported degradation mechanism involving moisture that is described by the following reversible reactions:

$$C_4H_9NH_3^+ + H_2O \rightarrow C_4H_9NH_2\uparrow + H_3O^+ \quad (2)$$

$$H_3O^+ + Br^- \rightarrow HBr\uparrow + H_2O \quad (3)$$

Owing to the strong hydrogen bonding between water and organic cations or halide, water molecules can easily penetrate into the interlayers of inorganic frameworks, as shown in Figure 5. In the case of halide vacancies, it can be also generated before the generation of organic vacancies because of the low formation energy of both vacancies. However, the halide or organic cation vacancies are charged defects (halide vacancy, positive charged defect; organic cation vacancy, negative charged defect), which lead to the elimination of oppositely charged ions for charge balance. These vacancies accelerate the destruction of the perovskite structure. Thus, the 2D halide perovskite structure is totally destroyed after Br elimination. Considering the defect tolerance property of the perovskite, before reaching certain defects densities, it can maintain PL and white emission even if the intensities significantly decrease. The reaction of water with butylammonium occurred over several water molecules positioned at OHP lattices. Consequently, the organic cation vacancies were formed by the evaporation of the produced amine.[47]

In conclusion, white luminescence of $(BuA)_2PbBr_4$ arose from defect-assisted recombination, as confirmed by IR nanoscopy and power-dependent PL measurements, and the moisture between the layers was closely related to the defect generation. We prepared (100) perovskite sheets by controlling the concentration and mixing ratio of solvents with different solubility. Additionally, we observed unique broadband emission and revealed its origin by performing power-dependent PL measurements and IR nanoscopy. The broadband emission in (100) perovskite was generated by the organic cation vacancies. This is distinct from the self-trapped excitons at small polaron states in (110) and (111) perovskites. We expect that the proposed origin of white-light emission will provide an understanding of the variation of the optical properties according to structural modulation and contribute to the fabrication of high-performance OHP-based optoelectronic devices.[48]

EXPERIMENTAL SECTION

Materials and Sample Preparation. *n*-Butylammonium bromide ($C_4H_9NH_3Br$, BuABr) was purchased from GreatCell Solar. Lead(II) bromide ($PbBr_2$, > 98%) and organic solvents such as DMSO (>99.5%, ACS reagent), acetonitrile (CH_3CN, 99.5%, ACS reagent), and chlorobenzene (C_6H_6Cl, > 99.5%, ACS reagent) were obtained from Sigma-Aldrich. All chemicals were used without further purification. For the $(BuA)_2PbBr_4$ microsheet preparation, a 1 M precursor solution was prepared by mixing BuABr:$PbBr_2$ in 1 mL DMSO, at a molar ratio of 2:1. The precursor solution was diluted by a factor of 1375 with acetonitrile (~0.73 mM). The diluted solution (0.5 mL) was mixed with chlorobenzene (0.3 mL) for preparing the coating solution. The coating solution (10 μL) was drop-casted on a preheated SiO_2 substrate (1 × 1 cm^2) at 80 °C. The $(BuA)_2PbBr_4$ microsheets were annealed for 10 min to remove the solvents. The entire process was conducted under ambient (21 °C) conditions.

AFM and IR Nanoscopy. The 2D perovskite fixed on ZnSe prime substrates was analyzed in the spectral range of 1100−3800 cm^{-1} via IR nanoscopy (Anasys Instruments, United States) with bottom-up illumination and a tunable IR source (optical parametric oscillator, Ekspla, Lithuania). The samples were scanned in the contact mode at a scan rate of 0.05 Hz using a gold-coated AFM tip (Anasys Instruments, United States). IR absorbance images and AFM images were simultaneously recorded for the same regions. Chemical mapping was performed using 3200 cm^{-1} excitation sources. Additionally, it was reconstructed using an integrated nano-IR software (Analysis Studio v3.7, Anasys Instruments, United States).

PL Mapping of Optical Properties. All the measurements were performed at room temperature (21 °C), and in order to minimize the influence of moisture present in the atmospheric environment, a rotary vacuum pump was used to create a vacuum of about 9 × 10^{-3} Torr; the experiment was then conducted in an inert atmosphere using argon gas. Confocal PL spectroscopy (NT-MDT, Russia) and a confocal micro-PL setup (Witec, Germany) were used to excite the sample with a continuous-wave laser (λ = 355 and 375 nm) that was focused using a 40× objective lens (numerical aperture = 0.75).

ASSOCIATED CONTENT

Supporting Information

The Supporting Information is available free of charge at https://pubs.acs.org/doi/10.1021/acs.jpclett.9b03328.

Additional discussion of the data and Figures S1−S6 (PDF)

AUTHOR INFORMATION

Corresponding Author

*E-mail: mjeong@skku.edu.

ORCID

Dae Young Park: 0000-0002-6162-9553
Chanwoo Lee: 0000-0001-7630-2927
Duc Anh Nguyen: 0000-0001-8021-9667
Mun Seok Jeong: 0000-0002-7019-8089

Author Contributions

⊥D.Y.P. and S.-J.A. contributed equally to this work. D.Y.P., S.-J.A., and M.S.J. designed the experiments. D.Y.P., S.-J.A., and C.L. conducted the synthesis and optical analysis experiments. D.Y.P., S.-J.A., and M.S.J. analyzed the results and wrote the manuscript. All authors discussed the results and commented on the manuscript.

Notes

The authors declare no competing financial interest.

DOI: 10.1021/acs.jpclett.9b03328
J. Phys. Chem. Lett. 2019, 10, 7942−7948

■ ACKNOWLEDGMENTS

This work was supported by IBS-R011-D1 and a National Research Foundation of Korea (NRF) grant funded by the Korean government Ministry of Science and ICT (MSIT) (NRF-2019M3D1A1078296 and NRF-2019R1A2B5B02070657).

■ REFERENCES

(1) Petrus, M. L.; Schlipf, J.; Li, C.; Gujar, T. P.; Giesbrecht, N.; Müller-Buschbaum, P.; Thelakkat, M.; Bein, T.; Hüttner, S.; Docampo, P. Capturing the Sun: A Review of the Challenges and Perspectives of Perovskite Solar Cells. *Adv. Energy Mater.* **2017**, *7* (16), 1700264.

(2) Sutherland, B. R.; Sargent, E. H. Perovskite photonic sources. *Nat. Photonics* **2016**, *10*, 295.

(3) Adjokatse, S.; Fang, H.-H.; Loi, M. A. Broadly tunable metal halide perovskites for solid-state light-emission applications. *Mater. Today* **2017**, *20* (8), 413−424.

(4) Saouma, F. O.; Park, D. Y.; Kim, S. H.; Jeong, M. S.; Jang, J. I. Multiphoton Absorption Coefficients of Organic−Inorganic Lead Halide Perovskites $CH_3NH_3PbX_3$ (X = Cl, Br, I) Single Crystals. *Chem. Mater.* **2017**, *29* (16), 6876−6882.

(5) Park, D. Y.; Byun, H. R.; Lee, A. Y.; Choi, H. M.; Lim, S. C.; Jeong, M. S. Synthesis and Characterization of Bandgap-modulated Organic Lead Halide Single Crystals. *J. Korean Phys. Soc.* **2018**, *73* (11), 1716−1724.

(6) Yuan, M.; Quan, L. N.; Comin, R.; Walters, G.; Sabatini, R.; Voznyy, O.; Hoogland, S.; Zhao, Y.; Beauregard, E. M.; Kanjanaboos, P.; et al. Perovskite energy funnels for efficient light-emitting diodes. *Nat. Nanotechnol.* **2016**, *11*, 872.

(7) Li, X.; Ke, W.; Traoré, B.; Guo, P.; Hadar, I.; Kepenekian, M.; Even, J.; Katan, C.; Stoumpos, C. C.; Schaller, R. D.; et al. Two-Dimensional Dion−Jacobson Hybrid Lead Iodide Perovskites with Aromatic Diammonium Cations. *J. Am. Chem. Soc.* **2019**, *141* (32), 12880−12890.

(8) Cortecchia, D.; Yin, J.; Petrozza, A.; Soci, C. White light emission in low-dimensional perovskites. *J. Mater. Chem. C* **2019**, *7* (17), 4956−4969.

(9) Dohner, E. R.; Jaffe, A.; Bradshaw, L. R.; Karunadasa, H. I. Intrinsic White-Light Emission from Layered Hybrid Perovskites. *J. Am. Chem. Soc.* **2014**, *136* (38), 13154−13157.

(10) Hu, T.; Smith, M. D.; Dohner, E. R.; Sher, M.-J.; Wu, X.; Trinh, M. T.; Fisher, A.; Corbett, J.; Zhu, X. Y.; Karunadasa, H. I.; et al. Mechanism for Broadband White-Light Emission from Two-Dimensional (110) Hybrid Perovskites. *J. Phys. Chem. Lett.* **2016**, *7* (12), 2258−2263.

(11) Thirumal, K.; Chong, W. K.; Xie, W.; Ganguly, R.; Muduli, S. K.; Sherburne, M.; Asta, M.; Mhaisalkar, S.; Sum, T. C.; Soo, H. S.; et al. Morphology-Independent Stable White-Light Emission from Self-Assembled Two-Dimensional Perovskites Driven by Strong Exciton−Phonon Coupling to the Organic Framework. *Chem. Mater.* **2017**, *29* (9), 3947−3953.

(12) Mao, L.; Wu, Y.; Stoumpos, C. C.; Traore, B.; Katan, C.; Even, J.; Wasielewski, M. R.; Kanatzidis, M. G. Tunable White-Light Emission in Single-Cation-Templated Three-Layered 2D Perovskites $(CH_3CH_2NH_3)_4Pb_3Br_{10-x}Cl_x$. *J. Am. Chem. Soc.* **2017**, *139* (34), 11956−11963.

(13) Zhu, X. Y.; Podzorov, V. Charge Carriers in Hybrid Organic−Inorganic Lead Halide Perovskites Might Be Protected as Large Polarons. *J. Phys. Chem. Lett.* **2015**, *6* (23), 4758−4761.

(14) Feynman, R. P. Slow Electrons in a Polar Crystal. *Phys. Rev.* **1955**, *97* (3), 660−665.

(15) Fröhlich, H. Electrons in lattice fields. *Adv. Phys.* **1954**, *3* (11), 325−361.

(16) Ivanovska, T.; Dionigi, C.; Mosconi, E.; De Angelis, F.; Liscio, F.; Morandi, V.; Ruani, G. Long-Lived Photoinduced Polarons in Organohalide Perovskites. *J. Phys. Chem. Lett.* **2017**, *8* (13), 3081−3086.

(17) Cortecchia, D.; Yin, J.; Bruno, A.; Lo, S.-Z. A.; Gurzadyan, G. G.; Mhaisalkar, S.; Brédas, J.-L.; Soci, C. Polaron self-localization in white-light emitting hybrid perovskites. *J. Mater. Chem. C* **2017**, *5* (11), 2771−2780.

(18) Yin, J.; Li, H.; Cortecchia, D.; Soci, C.; Brédas, J.-L. Excitonic and Polaronic Properties of 2D Hybrid Organic−Inorganic Perovskites. *ACS Energy Letters* **2017**, *2* (2), 417−423.

(19) Yangui, A.; Pillet, S.; Bendeif, E.-E.; Lusson, A.; Triki, S.; Abid, Y.; Boukheddaden, K. Broadband Emission in a New Two-Dimensional Cd-Based Hybrid Perovskite. *ACS Photonics* **2018**, *5* (4), 1599−1611.

(20) Wang, S.; Yao, Y.; Kong, J.; Zhao, S.; Sun, Z.; Wu, Z.; Li, L.; Luo, J. Highly efficient white-light emission in a polar two-dimensional hybrid perovskite. *Chem. Commun.* **2018**, *54* (32), 4053−4056.

(21) Zhai, Y.; Baniya, S.; Zhang, C.; Li, J.; Haney, P.; Sheng, C.-X.; Ehrenfreund, E.; Vardeny, Z. V. Giant Rashba splitting in 2D organic-inorganic halide perovskites measured by transient spectroscopies. *Science Advances* **2017**, *3* (7), No. e1700704.

(22) Ghosh, D.; Smith, A. R.; Walker, A. B.; Islam, M. S. Mixed A-Cation Perovskites for Solar Cells: Atomic-Scale Insights Into Structural Distortion, Hydrogen Bonding, and Electronic Properties. *Chem. Mater.* **2018**, *30* (15), 5194−5204.

(23) Wu, B.; Yuan, H.; Xu, Q.; Steele, J. A.; Giovanni, D.; Puech, P.; Fu, J.; Ng, Y. F.; Jamaludin, N. F.; Solanki, A.; et al. Indirect tail states formation by thermal-induced polar fluctuations in halide perovskites. *Nat. Commun.* **2019**, *10* (1), 484.

(24) Dou, L.; Wong, A. B.; Yu, Y.; Lai, M.; Kornienko, N.; Eaton, S. W.; Fu, A.; Bischak, C. G.; Ma, J.; Ding, T.; et al. Atomically thin two-dimensional organic-inorganic hybrid perovskites. *Science* **2015**, *349* (6255), 1518.

(25) Yang, W. S.; Noh, J. H.; Jeon, N. J.; Kim, Y. C.; Ryu, S.; Seo, J.; Seok, S. I. High-performance photovoltaic perovskite layers fabricated through intramolecular exchange. *Science* **2015**, *348* (6240), 1234.

(26) Green, M. A.; Ho-Baillie, A.; Snaith, H. J. The emergence of perovskite solar cells. *Nat. Photonics* **2014**, *8*, 506.

(27) Jeon, N. J.; Noh, J. H.; Kim, Y. C.; Yang, W. S.; Ryu, S.; Seok, S. I. Solvent engineering for high-performance inorganic−organic hybrid perovskite solar cells. *Nat. Mater.* **2014**, *13*, 897.

(28) Li, Y. Y.; Lin, C. K.; Zheng, G. L.; Cheng, Z. Y.; You, H.; Wang, W. D.; Lin, J. Novel ⟨110⟩-Oriented Organic−Inorganic Perovskite Compound Stabilized by N-(3-Aminopropyl)imidazole with Improved Optical Properties. *Chem. Mater.* **2006**, *18* (15), 3463−3469.

(29) Smith, M. D.; Jaffe, A.; Dohner, E. R.; Lindenberg, A. M.; Karunadasa, H. I. Structural origins of broadband emission from layered Pb−Br hybrid perovskites. *Chemical Science* **2017**, *8* (6), 4497−4504.

(30) Smith, M. D.; Karunadasa, H. I. White-Light Emission from Layered Halide Perovskites. *Acc. Chem. Res.* **2018**, *51* (3), 619−627.

(31) Byun, H. R.; Park, D. Y.; Oh, H. M.; Namkoong, G.; Jeong, M. S. Light Soaking Phenomena in Organic−Inorganic Mixed Halide Perovskite Single Crystals. *ACS Photonics* **2017**, *4* (11), 2813−2820.

(32) Schmidt, T.; Lischka, K.; Zulehner, W. Excitation-power dependence of the near-band-edge photoluminescence of semiconductors. *Phys. Rev. B: Condens. Matter Mater. Phys.* **1992**, *45* (16), 8989−8994.

(33) Taguchi, T.; Shirafuji, J.; Inuishi, Y. Excitonic emission in cadmium telluride. *Phys. Status Solidi B* **1975**, *68* (2), 727−738.

(34) Dazzi, A.; Prater, C. B.; Hu, Q.; Chase, D. B.; Rabolt, J. F.; Marcott, C. AFM−IR: Combining Atomic Force Microscopy and Infrared Spectroscopy for Nanoscale Chemical Characterization. *Appl. Spectrosc.* **2012**, *66* (12), 1365−1384.

(35) Dazzi, A.; Prater, C. B. AFM-IR: Technology and Applications in Nanoscale Infrared Spectroscopy and Chemical Imaging. *Chem. Rev.* **2017**, *117* (7), 5146−5173.

(36) Marcott, C.; Lo, M.; Kjoller, K.; Prater, C.; Gerrard, D. P. Applications of AFM-IR—Diverse Chemical Composition Analyses at Nanoscale Spatial Resolution. *Microsc. Today* **2012**, *20* (6), 16−21.

DOI: 10.1021/acs.jpclett.9b03328
J. Phys. Chem. Lett. 2019, 10, 7942−7948

(37) Guo, X.; McCleese, C.; Gao, W.; Wang, M.; Sang, L.; Burda, C. Investigation of moisture stability and PL characteristics of terpineol-passivated organic−inorganic hybrid perovskite. *Materials for Renewable and Sustainable Energy* **2016**, *5* (4), 17.
(38) Rashad, M. M.; Elseman, A. M.; Hassan, A. M. Facile synthesis, characterization and structural evolution of nanorods single-crystalline $(C_4H_9NH_3)_2PbI_2X_2$ mixed halide organometal perovskite for solar cell application. *Optik* **2016**, *127* (20), 9775−9787.
(39) Mojet, B. L.; Ebbesen, S. D.; Lefferts, L. Light at the interface: the potential of attenuated total reflection infrared spectroscopy for understanding heterogeneous catalysis in water. *Chem. Soc. Rev.* **2010**, *39* (12), 4643−4655.
(40) Zhang, L.; Liu, X.; Li, J.; McKechnie, S. Interactions between molecules and perovskites in halide perovskite solar cells. *Sol. Energy Mater. Sol. Cells* **2018**, *175*, 1−19.
(41) Song, Z.; Zhao, J.; Liu, Q. Luminescent perovskites: recent advances in theory and experiments. *Inorg. Chem. Front.* **2019**, *6*, 2969−3011.
(42) Bischak, C. G.; Hetherington, C. L.; Wu, H.; Aloni, S.; Ogletree, D. F.; Limmer, D. T.; Ginsberg, N. S. Origin of Reversible Photoinduced Phase Separation in Hybrid Perovskites. *Nano Lett.* **2017**, *17* (2), 1028−1033.
(43) Shirayama, M.; Kato, M.; Miyadera, T.; Sugita, T.; Fujiseki, T.; Hara, S.; Kadowaki, H.; Murata, D.; Chikamatsu, M.; Fujiwara, H. Degradation mechanism of CH3NH3PbI3 perovskite materials upon exposure to humid air. *J. Appl. Phys.* **2016**, *119* (11), 115501.
(44) Cheng, Y.-B.; Han, Y.; Braunger, S.; Dkhissi, Y.; Weber, K.; Pringle, J.; Bach, U.; Spiccia, L. Degradation observations of encapsulated planar $CH_3NH_3PbI_3$ perovskite solar cells at high temperatures and humidity. *J. Mater. Chem. A* **2015**, *3*, 8139.
(45) Huang, J.; Tan, S.; Lund, P.; Zhou, H. Impact of H_2O on organic-inorganic hybrid perovskite solar cells. *Energy Environ. Sci.* **2017**, *10*, 2284.
(46) Jana, A.; Kim, K. S. Effect of Organic−Cation Exchange Reaction of Perovskites in Water: H-Bond Assisted Self-Assembly, Black Phase Stabilization, and Single-Particle Imaging. *ACS Applied Energy Materials* **2019**, *2* (6), 4496−4503.
(47) Stoumpos, C. C.; Cao, D. H.; Clark, D. J.; Young, J.; Rondinelli, J. M.; Jang, J. I.; Hupp, J. T.; Kanatzidis, M. G. Ruddlesden−Popper Hybrid Lead Iodide Perovskite 2D Homologous Semiconductors. *Chem. Mater.* **2016**, *28* (8), 2852−2867.
(48) Zhou, N.; Yang, R.; Zhai, T. Two-dimensional non-layered materials. *Materials Today Nano* **2019**, *8*, 100051.

DOI: 10.1021/acs.jpclett.9b03328
J. Phys. Chem. Lett. 2019, 10, 7942−7948